Title	Evaluation and analysis of fracture modes in single composite basalt/epoxy fibres by photoelastic method and single fibre fragmentation test
Author(s)	Thornton, Eoghan; Ghabezi, Pouyan; Strain, Findhan; Harrison, Noel M.
Publication Date	2022-04-11
Publication Information	Thornton, Eoghan, Ghabezi, Pouyan, Ralph, Calvin, Strain, Findhan, & Harrison, Noel M. (2022). Evaluation and Analysis of Fracture Modes in Single Composite Basalt/Epoxy Fibres by Photoelastic Method and Single Fibre Fragmentation Test. Fibers and Polymers, 23(5), 1396-1409. doi:10.1007/s12221-022-4597-y
Publisher	Springer
Link to publisher's version	https://doi.org/10.1007/s12221-022-4597-y
Item record	http://hdl.handle.net/10379/17422
DOI	http://dx.doi.org/10.1007/s12221-022-4597-y

Evaluation and Analysis of Fracture Modes in single Composite Basalt/Epoxy Fibres by Photoelastic Method and Single Fibre Fragmentation Test

Eoghan Thornton [3], Pouyan Ghabezi* [1, 2, 3], Calvin Ralph [4], Findhan Strain [5], Noel M Harrison [1, 2, 3, 6]

[1] IComp Irish Composites Centre, Limerick, V94 T9PX, Ireland,

[2] I-Form Advanced Manufacturing Research Centre, Dublin, D04 V1W8, Ireland

[3] Mechanical Engineering, National University of Ireland, Galway, H91 TK33, Ireland,

[4] Mechanical Engineering, School of Engineering, Ulster University, Belfast, BT37 0QB Northern Ireland,

[5] Director, Comeragh Composites, Belfast, BT9 6PP, Northern Ireland,

[6] Ryan Institute for Environmental, Marine and Energy Research, NUI Galway, Galway, H91 TK33, Ireland,

* Corresponding author: Email: pouyan.ghabezi@nuigalway.ie,

Abstract:

In this work, the suitability of basalt fibres for uni-directional composite material applications, and adhesion between the fibres and the matrix they are embedded in have been investigated. A single fibre fragmentation test was carried out on 13µm diameter basalt fibres embedded in a dog-bone epoxy matrix. Photoelastic analysis was used to observe different fracture mechanisms in a single fibre composite sample and fibre breaks during testing. A theoretical model based on a Griffith's fracture mechanics approach was used to determine the fibre-matrix interfacial shear strength, which is a measurement of the level of adhesion between the fibre and the matrix. It was also used to predict the fibre fragment axial stress and the fragment interfacial shear stress, both as functions of axial position on the fibre. A finite element model was developed to simulate the fibre fracture process, and the redistribution of stresses in the fibre and the local region surrounding a fibre break. The developed experimental procedure was successful in that stress-induced birefringence was observed in the tested samples, as well as the characteristic shear stress light fringes that occur in the regions surrounding fibre fractures. Also, there were some similarities between the finite element model results and the theoretical predictions. The critical fibre length, l_c was measured as 0.752 mm, whereas this value was calculated 0.6708 mm from finite element predicted interfacial shear stress distribution for fibre fragment. A combination of all three types of failure modes was recorded across the samples that were tested, while only a single failure mode was observed in the finite element model. According to the theoretical model, for a given set of parameters and constant stress with only the fibre length varying, the axial stress in the fibre reduces as the fibre gets smaller.

Keywords: Basalt fibre, Photoelastic, Fracture mode, Single Fibre Fragmentation Test, Finite Element Modeling.

1. Introduction

Today, basalt fibres can be considered the ‘new-comer’ to the composite industry. There is a wide range of material properties associated with basalt fibres which make it a desirable composite material. Some research has been done on fracture behaviour of composite materials to characterize their strength and resistance against different loadings [1]. An important characteristic of uni-directional composites is the level of adhesion at the interface between the fibre and the matrix. When uni-directional composites are subjected to a tensile load parallel to the fibre direction, stress is transferred from the matrix to the fibre via shear [2]. As the load increases, the fibre fractures into smaller lengths. At a certain point, the fibres are unable to fracture any further, as they essentially lose their load-bearing capacity. This point is called fibre saturation, and the fibre fragment length at this point is known as the critical fibre length. The critical transfer length is required for the interfacial shear stress to load the fibre to its fracture stress. Fibres with a shorter length than this embedded in the matrix will pull out. One interesting feature of composites containing chopped fibres is that they are almost as strong as those containing continuous fibres; providing the fibres exceed a critical length. Fibres shorter than the critical length will not carry their maximum load are thus unable to function effectively. Beyond the critical length, the fibres will carry an increasing fraction of the applied load and may fracture before the matrix especially if the matrix material has some ductility eg. a thermoplastic such as PEEK or a metal matrix. It is therefore necessary to determine what the critical fibre length is. Shear stress is used to transfer the applied load to the fibre - so that the fibre can do its job and the tensile stress that results from this in the fibre is not the same along the length of the fibre - in fact, it increases from zero at the free end to some arbitrary value in the middle of the fibre then decreases as towards the other free end. A high level of adhesion is desirable in a composite, as it represents a good stress transfer mechanism from the matrix to the fibre. This allows for a significant portion of the load to be borne by the fibres, which have a much higher tensile strength and modulus than the matrix [2]. Single-fibre fragmentation test (SFFT) is the most widely used to evaluate interface properties in single-fibre composites, due to its ease of testing, relatively simple preparation of samples [3].Wang et al [4] have carried out an SFFT test on carbon fibre-epoxy single fibre composites. A finite element model of the fibre failure process was also developed. The finite element model created was a 2-D planar model of a short section of the fibre and the surrounding matrix, and it was assumed that the fibre and matrix are perfectly bonded. Van der Meer et al. [5] have presented a numerical investigation into one of the tests that has been proposed for measuring interfacial properties between fibre and matrix. They have introduced a new cohesive zone model with friction, as well as an original numerical framework for modelling embedded fibres. Their research has generated new insight into the meaning of the single fibre fragmentation test, confirming the applicability of shear lag theory also in presence of multiple cracks, and emphasizing the relevance of matrix plasticity for the development of friction in the test. Sørensen [6] has developed a shear-lag model utilizing the relation for the loss in potential energy of Budiansky, Hutchinson and Evans for the analysis of single fibre fragmentation tests for the characterization of the mechanical properties of the fibre/matrix interface in composite materials. Stojcevski et al. [7] have carried out single fibre fragmentation, Iosipescu and short beam shear testing to evaluate the translatability and sensitivity of interfacial shear strength across micro-, meso- and macro-scale testing protocols. Humbert et al. [8] proposed an exact solution for the characterization of thermal stresses in a single-fibre composite of finite length that involves a particular solution that is added to a three-dimensional complementary displacement field which satisfies automatically the Navier's equations. Kant and Penumadu [9] have measured the fracture toughness of single Toray T700 polyacrylonitrile carbon fibres using focused ion beam (FIB) nano-fabrication techniques to induce controlled geometry of end notches with lengths 100 nm to 1 μm. These fibres were subjected to axial loading with a nano-tensile testing system for evaluating mode I fracture behaviour. The influence of the basalt fibre's length and content on the fundamental mechanical properties of concrete has been investigated Sun et al. [10] using multi-scale simulation. A damage constitutive model was developed at the mesoscopic scale in accordance with the Mori-Tanaka homogenization theory and progressive damage theory to predict the composite material properties of basalt fibre reinforced concrete. At the macroscopic scale, the obtained material properties of basalt fibre reinforced concrete from mesoscopic were input into the finite element specimen model to simulate the mechanical performance of these materials. Sarasini et al., [11] have presented an experimental investigation of the effects of temperature and atmosphere on the tensile behaviour of basalt fibres. The properties of basalt fibres range from somewhere between E and S-glass fibres to slightly better than S-glass. It is worth noting that the cost of manufacturing for basalt fibres is less than that for S-glass fibres, making it a potential replacement for S-glass fibres [12]. A study carried out at Leuven University, Belgium, compared unidirectional E-glass and basalt fibre composites with a fibre volume fraction of 40% by subjecting them to a three-point bending test and an interlaminar shear strength test. The basalt fibre composite strength was recorded as 13.7% higher than that of the E-glass fibre composite, while the basalt fibre composite stiffness was 17.5% greater than the stiffness of the E-glass fibre composite [13]. Meng et al [14] conducted a series of experiments to develop continuous basalt fibres using two natural forms of basalt. The average tensile strength of the fabricated continuous basalt fibres was 4.1GPa. They revealed that the amount of glass network modifier ($Na_2O + K_2O$) has a negative correlation with the tensile strength of continuous basalt fibres. Sabet et al. [15] have investigated the tensile strength of basalt fibres at room temperature and also after exposure to 300, 350, 400, 450 and 500 °C in a furnace for durations of 5, 10, 15 and 20 minutes. The results showed that the residual strength of basalt fibres drastically decreases after 20 min exposure at 300 and 400 °C and is only about 57% and 35% of that of fibres at room temperature, respectively. Eslami Farsani et al. [16] have studied the effects of thermal cycles on hardness and impact resistance of three types of phenolic-matrix composites, phenolic resin reinforced with (1) woven basalt fibres, (2) woven carbon fibres and (3) hybrid of basalt and carbon fibres. Akhlaghi et al. [17] have shown the applicability of basalt fibre as a reinforcing material for metal matrix composites through various experimental works for thermal stability and mechanical properties.

In this work, the goal is to determine the tensile load-bearing capability and fracture behaviour of basalt fibres for composite material applications. Whilst the properties and cost of basalt fibres suggest that they are a good choice for composite fibres, more information is required on the quality of adhesion between the fibres and the matrix they are embedded in.

In this research, a single fibre fragmentation test was performed on single fibre basalt-epoxy dog-bone samples, with the objective of characterising the interfacial adhesion and critical fibre length in single basalt fibre through observing the different fibre failure modes via photoelastic methods. A theoretical model which uses Griffith's fracture mechanics approach was used to quantify the interfacial adhesion in terms of interfacial shear strength. Finally, a finite element model was created to simulate the fibre failure process, finding critical fibre length, and failure modes.

2. Experimental

2.1. Experimental Testing

For the experimental testing in this research, a single fibre fragmentation test was carried out. The photoelastic analysis method is the most common technique used to determine the stresses at which a certain break occurs. The objective of this technique is to observe stress-induced birefringence, which occurs in transparent materials which are optically non-isotropic, in the region surrounding a fibre break and matching it with the stress at which it occurred. For fibre breaks to be accurately matched with the stresses at which they occur, incremental loading must be implemented [18]. After the application of a load, the gauge length can be scanned for the presence of any new fibre breaks before applying the next incremental load. The fibre diameter of each sample also needed to be accurately measured to carry out theoretical calculations.

2.2. Materials

The samples tested in this research were supplied by Comeragh Composites, Northern Ireland. The samples consist of a single 13 μm diameter basalt fibre embedded in a dog-bone shape epoxy matrix. The basalt fibres used were manufactured by Mafic, located in Kells, Co.

Meath, Ireland. The epoxy matrix used was a low viscosity, two-part epoxy resin (RS-M135 with a slow hardener, RS-MH137), which is a product of PRF Composite Materials, Poole, Dorset, England (Table 1). In order to embed the single basalt fibres into the epoxy matrix, a dog-bone mould was designed and the single fibres were fixed in the middle of the mould (Figure 1) within a slight tensile load to make sure the fibre does not get bent during adding the epoxy and the hardener to the die ad curing process. Also, the approximate sample dimensions are shown in Figure 1.

Suggested position for Table 1

Suggested position for Figure 1

2.3. Sample Preparation

A simple sample holder was constructed from match-sticks, small pieces of plywood, foam, and a container to prevent the samples from being damaged or scratched. The first step taken at the outset of the experimental testing was to observe the samples under a microscope to view the fibre. While the fibres were visible to the naked eye under certain lighting conditions, and clearly visible using a magnifying glass, when viewed under a microscope the fibre could not be observed. This was due to microscopic imperfections on the epoxy, increasing the surface roughness and resulting in the epoxy being too opaque for the lens to penetrate it. Various levels of sample illumination were used to try and overcome this, such as cleaning them with isopropyl alcohol, followed by polishing them using a polishing compound, applying Isopropyl alcohol, polishing using a Parkside PABSW B2 10.8V, 1.3Ah electric drill with a mini polishing pad, etc., but the microscope lens was unable to focus on the fibre due to surface imperfections. Finally, the sample preparation procedure which resulted in the desired surface finish was carried out in a 'Beuhler Beta Grinder-Polisher'. The polishing compound used with the sample was a 'Beuhler Masterprep 0.05 Micron Diamond Polishing Suspension'. The samples were polished until the surface observed under the microscope was considered satisfactory.

2.4. Measurement Of Fibre Diameter

The fibre diameters were measured using an Olympus toolmakers microscope. The fibre diameters were measured under an X40 Olympus MSPlan20 lens and an Infinity camera attached, using the ocular crosshairs and stage displacement output. To calibrate the Infinity camera with the Olympus X40 lens, measurements needed to be taken from a stage micrometer of known dimensions. The stage micrometer used consisted of squares with a period of 10μm, which were arranged in multiple arrays, each of which had a period of 500μm. Once an image of the micrometer stage had been captured with the Infinity camera, the 'Calibration' option was chosen in the Infinity Analyse software. The largest length possible was then measured for calibration.

2.5. Experimental Setup and Testing

The experimental setup is illustrated in Figure 2, and the experimental protocol was based on Hunston et al., n.d [19]. The complete experimental setup consists of: a tensile tester to load the samples in small increments; a white light source to illuminate the samples; two linear polarisers to polarise the light from the light source travelling through the sample so that stress-induced birefringence can be observed; an Infinity 2 camera with an X100 lens for monitoring and imaging of the fibre and sample; and a jack device to give the operator control over the vertical displacement of the Infinity camera, so that the entire gauge length can be examined. The tensile tester used was a hydraulic Instron 8874 with a 1kN load cell. As suggested by the experimental protocol developed by Hunston et al., n.d. [19], a strain of 0.2% was desired for each step. For a gauge length of 20 mm, this is equivalent to

0.04mm. No indication of the ideal crosshead speed is given in the test protocol, but the work of Awal et al. [20] has shown that the best results were obtained at a speed of 0.2mm/min. Once the test was initiated, the displacement reading was monitored until the displacement had increased by 0.04mm, at which point the crosshead was stopped. It is recommended [19] that each load hold increment last 10 minutes. This is to ensure that stresses in the matrix are transferred to fibre before commencing the next step. It is recommended that the sample be left for the first 8 minutes, with the final 2 minutes for checking the fibre for the occurrence of any new breaks. Once all samples had been tested, the fibres were analysed using the toolmaker's microscope to capture images of the fibre breaks and to record the fibre fragment lengths.

Suggested position for Figure 2

This section details how the finite element model was created and refined to generate an accurate simulation of the fibre break in the single fibre fragmentation process. This model does not simulate interfacial debonding or matrix damage. The following method is based on Wang et al. work [4] in 2010. The finite element software ABAQUS CAE was used to create the model, while the fibre breaks were simulated using the subroutine USDFLD. This stands for User Defined Field and was developed in MS Visual Studio 2013 using the programming language FORTRAN. Fibre and matrix in this research were considered to be homogeneous, isotropic, elastic materials [4]. The elastic material properties that were assigned to the fibre and the matrix are shown in Table 1. As modelling of a fibre repeatedly fracturing is non-linear, a small increment size was required to ensure that an accurate solution is obtained. Once the model and subroutine were running successfully, an increment convergence study was carried out. Using an unbiased mesh of the same size for each job, the increment size was gradually reduced. The Von Mises stress of the same three elements was taken from each job to determine increment convergence. Von Mises stress was used here as it incorporates all the principal stresses for each element. Figure 3 shows the entire mesh used for the increment convergence study.

Suggested position for Figure 3

The ratio of fibre to matrix elements used was 2:1, as seen in figure 3. From the results of the increment convergence study, it was evident that the solution converges at approximately 8000 increments. This increment size was selected as the final increment size and was then used for the mesh convergence study and final solution. Only two boundary conditions were required in the initial step of this model; the upper left and right-hand corners of the upper matrix section were constrained in the U2, or Y, direction. This was to prevent vertical displacement during tensile displacement of the model. With respect to loading, a tensile displacement load was applied to both ends of the model to simulate straining. The total displacement loading applied to the model was equivalent to 5% straining of the model. As the application of the displacement load was required at a constant rate, the ABAQUS default amplitude ramp was not suitable. Instead, a tabular amplitude was created, to give a linear application of displacement. Two initial conditions were also required to be defined in the input file to successfully run this model, as they are not supported in ABAQUS CAE. The initial condition types used were ‘FIELD’ and ‘SOLUTION’. FIELD is used to assign initial values of predefined field variables. This initial condition was used to set the value of the elastic modulus field variable at each fibre node to 1, representing an un-degraded elastic modulus. SOLUTION allows for the definition of the initial values of solution-dependent state variables. This was applied to the fibre elements, with the initial value set to 1. Similar to FIELD, the function of this initial condition was to ensure that the fibre modulus is not degraded prematurely. To increase the accuracy of modelling, meshing of both the fibre and matrix part instances utilised the same element type; a 4-node bilinear plane stress quadrilateral element, with reduced integration, and hourglass control (CPS4R). A mesh of medium fineness was used for the increment study, to achieve a good balance between accuracy and computational time. However, to obtain an accurate final solution, a mesh convergence study was also required. The method by which convergence was verified was slightly different than that used in the increment study, as element sizes will change with different meshes. Instead, the maximum Von Mises stresses for each mesh were compared. Firstly, several unbiased meshes coarser than that shown in figure 3 (4200 elements) were created. For the creation of meshes finer than that in figure 3, edge seed biasing was applied to the vertical matrix edges. The mesh bias direction was set towards the fibre. The minimum seed size was gradually reduced until the mesh elements close to the fibre were approximately the same height as the fibre elements. The minimum seed size was not reduced further as a mismatch between fibre and matrix element height was not desired. The results of the mesh convergence study show that mesh convergence occurs at 12750 elements.

The chosen theoretical model was that of Limin Zhou et al. [21], which is Griffith's fracture mechanics approach to the problem. This model is simplified slightly in this research, as the complete model requires knowledge of friction coefficients and residual clamping stresses due to matrix contraction and thermal shrinkage, which could not be determined. The procedure to determine the fibre tensile stress at the critical length and hence the interfacial shear strength from the SFFT is relatively simple and is outlined below. For a certain applied stress, σ_a, the fibre tensile stress, σ_f, as a function of fibre fragment axial position is determined from the following relationship [22]:

$$\sigma_f(z) = \eta\left(\sigma_a - \sigma_a \frac{\cosh\sqrt{A_1}z}{\cosh\sqrt{A_1}L}\right) \quad (1)$$

For fibre fragments of critical length, $2L = l_c$. As $\sigma_f(z)$ is maximised at the centre of the fibre fragment ($z = 0$, the fibre midpoint), the value for σ_f at this point is regarded as the fibre fragment tensile strength. A_1 and η are defined as [22] (Figure 4):

$$A_1 = \frac{2[\alpha + \gamma - 2k(\alpha v_f + \gamma v_m)]}{(1 + v_m)\left[2\gamma R^2 \ln\left(\frac{R}{a}\right) - a^2\right]} \quad (2)$$

$$\eta = \frac{1 - 2kv_m}{\alpha + \gamma - 2k(\alpha v_f + \gamma v_m)} \quad (3)$$

Where R is the radius of the matrix region affected by the fibre break and is measured from experimental images, and k, γ, and α are defined as [22]:

$$k = \frac{\alpha v_f + \gamma v_m}{\alpha(1 - v_f) + 2\gamma + v_m + 1} \quad (4)$$

$$\gamma = \frac{a^2}{R^2 - a^2} \quad (5)$$

$$\alpha = \frac{E_m}{E_f} \quad (6)$$

Suggested position for Figure 4

The interfacial shear strength, τ_i, is then determined using a modified Kelly-Tyson formula.

$$\tau_i = K\frac{\sigma_f(l_c)d}{2l_c} \quad (7)$$

Where K is a constant with a value of 0.75 as suggested by Ohsawa et al. [23].

The interfacial shear stress distribution along the fibre length Assuming a perfectly bonded interface after fibre fracture as a function of axial position, $\tau_f(z)$, is defined as [22]:

$$\tau_f(z) = \frac{a\sqrt{A_1}}{2}(\eta\sigma_a)\frac{\sinh\sqrt{A_1}z}{\cosh\sqrt{A_1}(L)} \quad (8)$$

5. Results and Discussion

5.1. Experimental Preparation Results

Table 2 shows the fibre diameter measurements taken using the Infinity 2 camera. Note that samples 4 and 5 contained two fibres. As there was no single fibre for measurement in these samples, they are marked n/a.

Suggested position for Table 2

From Table 2, it can be seen that of the nine samples that were prepared for incremental load testing, three samples were not suitable (samples 3, 4, and 5). Of the remaining six samples, two were not suitable for testing as the fibres contained within them had a diameter of ~15μm (samples 8 and 9). A further sample (sample 1) was deemed unsuitable due to internal imperfections in the matrix which made it impossible to clearly view the fibre under polarised light. This left three samples remaining for incremental load testing (samples 2, 6, and 7). The samples which were not considered suitable for testing were subjected to a tensile test with continuous loading (samples 1, 4, 8, and 9).

5.2. Testing Results

Figure 5 displays the force and displacement values that were recorded after the completion of each incremental loading step along with the total number of fibre breaks that were observed after the completion of each loading step (Table 3).

Suggested position for Figure 5

The load and displacement values were recorded from the Instron control interface. The lower values for sample 6 relative to samples 2 and 7 is a result of a software issue during testing which resulted in the loss of data for the first few incremental loads. For this reason, as well as no fibre fractures being observed during testing or when using the toolmaker's microscope to measure fibre fragment lengths, sample 6 was excluded from further analysis.

Suggested position for Table 3

Figure 6 shows images taken of sample 2 during progressive stages of the increment loading. As the images obtained during loading are similar for all samples, only sample 2 will be presented in detail. The average width of this sample was 3.917 mm, and this is marked in Figure 6 as a reference measurement. As different wavelengths/colours of light have different refractive indices, and due to the out-of-phase nature of the two light components, the colours of light in the components will undergo both destructive and constructive interference, resulting in the observed interference pattern. Figure 7 illustrates a uniform birefringent colour (stress-induced birefringence) in the gauge length, representing a single stress state (tensile stress) of sample 2 at various loading stages. Figure 8 shows samples 1, 4, 8, and 9 (continuous loading) after failure. As mentioned previously, there were imperfections present in sample 1. In fact, of the nine samples, five (including sample 1) contained similar imperfections that made monitoring of the fibre during testing virtually impossible. The continuous loading of sample 1 was monitored using the Infinity camera and recorded to observe what occurs to these imperfections under loading. Several still images from the video are presented below in Figure 9.

Suggested position for Figure 6

Suggested position for Figure 7

Suggested position for Figure 8

Suggested position for Figure 9

Transverse microcracks were observed on the surfaces of the samples after testing, which is indicative of the occurrence of fracture failure mode I (Figure 10) which was expected due to the nature of the tensile test. The presence of these microcracks, which were not present before testing, made it significantly more difficult to locate the fibre in the sample.

Suggested position for Figure 10

As mentioned above, there were micro imperfections present in numerous samples. Sample 1 was observed to see what happened to these imperfections under loading. It appeared that they grew in size and became more birefringent as the load increased. This is illustrated in Figure 9. These imperfections were even in samples where the fibre was monitored (Figure 6), although not to the same extent as other samples. Voids may form during the curing process. Polymerisation increases the mechanical properties of the resin, which coincides with volumetric shrinking. If a resin is cured in a constrained mould, which is likely the case with the samples used in this testing, it can adhere to the walls of the mould, which induces tensile stresses. If these tensile stresses exceed the epoxy resin strength at a given stage of curing, voids will form [24]. This is a possible explanation for the presence of micro imperfections. The presence of white spots under polarised light is akin to crazing in polymers. The fact that when monitored under increasing load and polarised light they increase in size suggests that they are indeed voids. This could also explain why numerous samples failed near or at the end of the gauge length. Failure in these regions is not thought to be due to a combination of stress states in these areas, as Figure 7 shows a uniform birefringent colour in the gauge length, representing a single stress state (tensile stress). As it can be seen, the colour diffraction trend has changed from load increment 14 (Figure 6 -D) to increment 18 (Figure 6 -E), a reason for this complies with local shear stresses which occur in the interface of fibre and matrix surrounding. There are a number of stresses present at the ends of the gauge length, which is evident by the multiple light fringes visible in Figure 9 (Right). These fringes can be used to determine the principal stresses and their directions, however doing so would have no benefit to this research as the region of interest is the gauge length. It is postulated that failure in these regions surrounding the end of the gauge length may be due to the coalescing of these voids which introduces a weak spot in the sample for failure to initiate. The fact that several samples fail in the region at or very close to the gauge length marker (Figure 8) could suggest that there is some feature in one of the moulds used which facilitates the formation of these voids in this particular region.

5.3. Fibre Fracture Results

Table 4 presents the number of breaks that were found using the toolmaker's microscope, as well as the fragment length. Table 5 then displays the failure mode associated with each break. Mode (a) represents a strong interface, with the fibre break propagating into the matrix and creating a disc-shaped transverse crack with little or no interfacial debonding. Mode (b) also represents a strong interface, but for a matrix that has a relatively lower shear strength capability than tensile strength. This mode may also be accompanied by interfacial debonding. Mode (c) is the result of a weak interface, with the fibre fracture accompanied by interfacial debonding in the region surrounding the break. Mode (a) is the desirable failure mode, as it represents the highest level of adhesion between the fibre and matrix, and hence the most efficient stress transfer from the matrix to the fibre.

Suggested position for Table 4

Suggested position for Table 5

Figure 11 illustrates the different fractures that were recorded in the samples. Not every fracture is presented here as some are quite similar. Table 5 and Figure 11 show that a combination of all three types of failure modes was recorded across the samples that were tested, with sample 9 presenting all three failure modes. This was an unexpected observation as it indicates a significant variation in fibre-matrix adhesion in a small area. This would be undesirable in a composite material, as it would result in certain regions pertaining to good stress transfer from the matrix to the fibre, whereas other regions in close proximity may be characterised by poor stress transfer. In these regions of poor stress transfer, the fibre is debonded from the matrix, and the fibre load-bearing capacity is dramatically reduced [22]. This increases the load carried by the matrix in that region. This variation in the level of adhesion may lead to the concentration of stress in certain areas of the matrix, which would result in premature failure of the composite in those areas, where the failure is governed mainly by the properties of the matrix material. However, except for sample 9, fibre failure mode (c) was not observed in any other samples. Failure modes (a) and (b) were distributed almost equally across all samples, which suggests a good interfacial bonding between the fibre and the matrix. It is worth noting that of the samples which were tested under polarising light (samples 2 and 7) with two fibre breaks observed visually, upon examination under a microscope three and four fractures were detected in samples 2 and 7, respectively. By comparing the failure modes of each break in these samples and the length of the fragments between them with the length between the breaks observed experimentally, it was concluded that all breaks that were observed experimentally were of failure mode (b).

Suggested position for Figure 11

This observation can be explained as follows. According to [24], failure mode (b) is characterised by a matrix that has a relatively lower shear than tensile strength capability. When a fibre fractures and strain energy is released and propagates through the local matrix region, the matrix is subject to local shear deformation as a result of failure mode (b). Failure mode (b) is often accompanied by a 'butterfly' shaped fracture as a result of this shear failure. Local shearing of the matrix about the fracture deforms the polymeric chains, which gives rise to multiple refractive indices as a result of molecular directional anisotropy. This is reinforced by the examination of Figure 6 (H), which shows a close-up image of the fracture shear stress birefringent patterns. It is observed in this figure that, if the fibre is taken as an axis at 0°, the birefringent shear stresses act approximately in the area from 315° to 45° (anti-clockwise direction) and 135° to 225° (anti-clockwise direction). This shows alignment with shear bands which suggests local shear yielding has occurred. However, in failure mode (a), there is a greater level of adhesion between the fibre and matrix. As strain energy is released after fracture, it results in a transverse crack that propagates perpendicular to the fibre axial direction. As the polymeric chains are broken by the crack, rather than deformed, this significantly reduces the deformation of the polymeric chains, hence the lack of stress-induced birefringence. With respect to samples 4 and 6 where no fibre breaks were observed, it is thought that the presence of two fibres in sample 4 influenced the fracture response. With sample 6, it is believed that the malfunction of the software had an impact on the loading of the sample. The formation of each failure mode depends on the interfacial properties of fibre and matrix, the presence of voids in the vicinity of the fibres, manufacturing quality, and consequently shear properties.

5.4. Processed Results

Table 6 gives information on testing temperature, and mechanical properties relating to each test.

Suggested position for Table 6

Stress-strain experimental results for samples loaded incrementally (samples 2 and 7) are derived, while samples 1, 4, 8, and 9 are subjected to continuous loading.

5.5. Finite Element Model Results

Figure 12 to Figure 15 (Left) show the S11 stress component in the FE model before and after each break event, while Figure 12 to Figure 15 (Right) plot the axial stress state in the fibre/fibre fragments against the length of the fibre before and after each fibre break event. The regions where the curves dip are the locations of fibre breaks. The line colours used in the graphs to represent the fibre stresses after fibre fracture for a certain break event are also used to represent the fibre stresses before fibre fracture for the following break event. This allows for an easy comparison of fibre stresses in different break events. As evident from the right side of Figure 12 to Figure 15 when a fibre fractures into two fragments, the maximum stresses in these fragments are reduced. Once one of these fragments fractures into a further two fragments, the maximum stresses in these two fragments are less than any other fragments previously. This is analogous to the reduction of the fibre tensile strength with decreasing fragment length. At what point the fibres stop fracturing in the FE model, this could be taken as an estimate of the critical length.

Suggested position for Figure 12

Suggested position for Figure 13

Suggested position for Figure 14

Suggested position for Figure 15

There are several limitations associated with model, which are a result of some assumptions made during the modelling process. The only failure mode observed in the model is (b), because: a perfectly bonded interface was assumed with no relative motion between the fibre and matrix, which does not allow for interfacial debonding (failure mode (c)); no damage model for the matrix was developed, and therefore no transverse cracks could propagate into the matrix (failure mode (a)). The shear stresses present in the entire model are shown in Figure 16. The interfacial shear stress at the fibre fragment interface was determined by creating a node path along one edge of a fibre fragment. The shear stress distribution along the fragment interface is plotted in Figure 17. The model accurately captures the shear stress distribution into the matrix about a fibre break, which is clearly evident when Figure 16 is compared with the experimental fracture shear stress distribution in Figure 6 (D). A butterfly-shaped distribution is observed, which is characteristic of failure mode (b). The model has also been able to successfully plot the shear stress distribution along a fibre fragment interface.

Suggested position for Figure 16

Suggested position for Figure 17

These findings show that the shear stress along the interface is zero at the fragment ends and is maximised a short distance from the fragment end before gradually decaying to zero at the fibre fragment midpoint. Using eq. (7), the interfacial shear strength for the fibre fragment shown in Figure 17 can be determined. Fibres shorter than the critical length will not carry their maximum load are thus unable to function effectively. Beyond the critical length, the fibres will carry an increasing fraction of the applied load and may fracture before the matrix especially if the matrix material has some ductility eg. a thermoplastic such as peek or a metal matrix. It is therefore necessary to determine what the critical fibre length is. The critical fibre length is defined as the shortest fibre fragment which can fracture with the application of stress

[25]. In other words, it is defined as the minimum length at which the centre of the fibre reaches the ultimate (tensile) strength σ_f, when the matrix achieves the maximum shear strength τ_m. The critical fibre length, l_c, therefore, was taken as the distance spanned by the curve in Figure 17, which is 0.6708 mm, and $\sigma_f(l_c)$ is the maximum value of the third green peak from the right in Figure 15, which is 2620 MPa. The resulting interfacial shear strength is presented in table 7 to allow for comparison with theoretical predictions. The FE model developed was considered successful in almost all aspects, based on the objective of the model and the assumptions made. It successfully models the fracture of the fibre into successively smaller fragments through the application of a displacement load to the matrix only, where internal matrix stresses are transferred to the fibre via shear. The maximum fibre tensile stress is located at the centre of the fibres, which is the point of fracture once the failure criterion is reached. This is shown in the plots of fibre axial stress in this section. This is the expected fracture location in experimental testing in the absence of fibre imperfections. However, in reality this is not always observed. In basalt fibres imperfections can occur as a result of cooling due to thermal contraction [12]. Some of the minerals that constitute basalt have different melting temperatures [26], which can also influence the uniformity of fibres when cooling.

5.6. Theoretical Results

Generation of results using the chosen theoretical model required knowledge of the following parameters: l_c, the critical fibre length, a, the fibre radius, R, the radius of the matrix region affected by the fibre fracture, and σ_a, the applied stress. Only results for samples 2 and 7 are presented here, as they were the only samples where fibre fractures were observed during experimental testing. As it could not be determined if either sample 2 or 7 reached saturation as only two fibre fractures were observed experimentally, l_c was taken as the minimum fibre fragment length that was recorded during single fibre fragment test. a was determined from the measurements given in table 2. σ_a was taken as the applied stress at the end of the step at which the second fibre fracture was observed.

R was determined by measuring the images taken of samples 2 and 7. As *R* is defined as the radius of the matrix region which is affected by the fibre break, this can be taken as the radius of sheared region surrounding the fibre break. The diameter of each shear region was measured, and average value was determined to use in the calculations. With these parameters determined, eqs. (1) through (7) can be used to determine the interfacial shear strength and to plot the tensile and shear stress distribution along a fibre fragment for samples 2 and 7, assuming a critical length of 0.752 mm in both cases from experimental work (table 4).

Table 7 gives the calculated interfacial shear strengths for the theoretical model and the FE model, while Figure 18 plots the tensile and shear stress distributions along a fibre fragment for samples 2 and 7. Figure 19 plots the axial stress distribution of the sample 7 fragment shown in Figure 18 (C), along with the stress distributions for fibre of decreasing length that are otherwise of the same dimensions as sample 7 and are subject to the same loading conditions.

Suggested position for Table 7

Suggested position for Figure 18

The FE model assumes that the tensile strength of the fibre is constant, when in fact it decreases as the fibre length decreases, as illustrated in Figure 19. Figure 19 plots the theoretical axial stress distribution of the sample 7 fragment shown in figure 18-C, along with the stress distributions for fibre of decreasing length that are otherwise of the same dimensions as sample 7 and are subject to the same loading conditions. The initial opening displacement is also quite large for the first break and is not considered representative of actual fibre failure. This is a result of the failure criterion and the initial length of the fibre. Before fibre fracture, the fibre is quite long. As load is transferred to the fibre, the load increases, with the maximum load at the centre of the fibre. However, due to the length of the fibre, several elements at the centre have very similar stresses and exceed the failure criterion simultaneously. The model also fails to capture the decay of the fibre fragment axial stress to zero at the fragment ends.

This is because when the elastic modulus is degraded for certain elements, it does not go to zero, and hence the degraded elements still pertain some load-bearing capacity. Based on a comparison of Figure 18, it is evident that this model is able to determine the fibre axial stress as a function of axial position for different fibres and matrices. Figure 19 illustrates that for a given set of parameters and constant stress with only the fibre length varying, the axial stress in the fibre reduces as the fibre gets smaller. This model can capture the decaying of the fragment interfacial shear stress to zero as the axial position approaches the midpoint of the fibre. Unlike the FE model, and similar to many other theoretical models, the chosen model does not predict zero shear stress at the fibre ends, but rather maximises it. However, similarities between the values for shear stress in the FE model and those predicted by the theoretical model for similar fragment lengths are evident. The same cannot be said for the comparison between the theoretical fibre fragment axial stress and that in the FE model, due to limitations of the FE model, which were discussed in the previous section.

Suggested position for Figure 19

7. CONCLUSION

A SFFT test was carried out on 13 µm basalt fibre-epoxy composite samples, and fracture behaviour (mode) of different samples were indicated. A Griffith's fracture mechanics approach was used to predict the interfacial shear strength, and the axial and shear stress distribution in a fibre fragment as a function of fragment axial position. The developed experimental procedure in this work was considered a success, although there were challenges with obtaining the desired results, in that stress-induced birefringence was observed in the tested samples, as well as the characteristic shear stress light fringes that occur in the regions surrounding fibre fractures. A 2-D planar FE model was also created to simulate the problem. The primary conclusions of the study are:

- From experimental tests, the critical fibre length, lc, was measured as 0.752 mm, whereas this value was calculated 0.6708 mm from FE predicted interfacial shear stress distribution for fibre fragment.
- It appeared that micro imperfections in the matrix surrounding fibres grew in size and became more birefringent as the load increased.
- A combination of all three types of failure modes (mode a, mode b, and mode c), were recorded across the samples. In contrast, only a single failure mode was observed in the model, failure mode (b), due to the lack of interface properties in the model or a damage model for the matrix.
- The FE model created was able to capture the transfer of stress from the matrix to the fibre via shear. The interfacial shear stress distribution along the fragment length was correctly predicted, with zero shear stress observed at both ends of the fragment, and at the midpoint.
- Theoretical fibre fragment interfacial shear stress as a function of fibre fragment axial position correctly captured the decay of shear stress to zero at the fibre fragment midpoint, but failed to predict zero shear stress at the fragment ends, instead maximising it.
- Some similarities between the FE model results and the theoretical predictions were observed.

Declarations

Conflict of interest: The authors declare that they have no known competing financial interests or personal relationships that could have appeared to influence the work reported in this paper.

REFERENCES

1. F. Hatami, M.R. Ayatollahi, A.R. Torabi, Limit curves for brittle fracture in key-hole notches under mixed mode I/III loading based on stress-based criteria, Eur. J. Mech. A Solids, 85, 104089, 2021.

2. S. Feih, K. Wonsyld, D. Minzari, P. Westermann, Testing Procedure for the Single Fiber Fragmentation Test, Risø National Laboratory for Sustainable Energy, Technical University of Denmark, Denmark, 1: 1-28, 2004.

3. D. Tripathi, F.R. Jones, Single Fibre Fragmentation Test for Assessing Adhesion in Fibre Reinforced Composites, J. Mater. Sci., 33(1): 1-16, 1998.

4. X. Wang, B. Zhang, S. Du, Y. Wu, X. Sun, Numerical simulation of the fiber fragmentation process in single-fiber composites, Mater. Des., 1980-2015, 31(5): 2464–2470, 2010.

5. F.P. Van der Meer, S. Raijmaekers, I.B.C.M. Rocha, Interpreting the single fibre fragmentation test with numerical simulations, Compos. Part A Appl. Sci. Manuf., 118: 259-266, 2019.

6. B.F. Sørensen, Micromechanical model of the single fiber fragmentation test, Mech. Mater., 104: 38-48, 2017.

7. F. Stojcevski, T.B. Hilditch, L.C. Henderson, A comparison of interfacial testing methods and sensitivities to carbon fiber surface treatment conditions, Compos. Part A Appl. Sci. Manuf., 118: 293-301, 2019.

8. L. Humbert, F. Colpo, J. Botsis, An axisymmetric stress analysis in a single fibre composite of finite length under a thermal expansion mismatch, Eur. J. Mech. A Solids, 28(2): 257-265, 2009.

9. M. Kant, D. Penumadu, Fracture behavior of individual carbon fibers in tension using nano-fabricated notches, Compos. Sci. Technol., 89: 83-88, 2013.

10. X. Sun, Z. Gao, P. Cao, C. Zhou, Mechanical properties tests and multiscale numerical simulations for basalt fiber reinforced concrete, Constr. Build. Mater., 202: 58-72, 2019.

11. F. Sarasini, J. Tirillò, M.C. Seghini, Influence of thermal conditioning on tensile behaviour of single basalt fibres, Compos. B. Eng., 132: 77-86, 2018.

12. K. Singha, A Short Review on Basalt Fibres, Int. J. Text. Sci., 1(4): 19–28, 2012.

13. A. Ross, Basalt Fibers: Alternative to Glass? https://www.compositesworld.com/articles/basalt-fibers-alternative-to-glass, (Accessed 15 February 2021).

14. Y. Meng, J. Liu, Y. Xia, W. Liang, Q. Ran, Z. Xie, Preparation and characterization of continuous basalt fibre with high tensile strength, Ceram. Int., 47: 9, pp 12410-12415, 2021.

15 S. Sabet, F. Akhlaghi, R. Eslami Farsani, The Effect of Thermal Treatment on Tensile Properties of Basalt Fibers, J. Ceram. Sci. Technol., 6(3): 245-248, 2015.

16 R. Eslami-Farsani, M.R. Khalili, M. Najafi, Effect of Thermal Cycling on Hardness and Impact Properties of Polymer Composites Reinforced by Basalt and Carbon Fibers, J. Therm. Stresses, 36 (7): 684-698. 2013.

17 F. Akhlaghi, R. Eslami-Farsani, SMM Sabet, Synthesis and Characteristics of Continuous Basalt Fiber Reinforced Aluminum Matrix Composites, J. Compos. Mater., 47(27): 3379-3388, 2013.

18. M.J. Rich, L.T. Drzal, , D.L. Hunston, G.A. Holmes, W.G. McDonough, Round Robin Assessment of the Single Fiber Fragmentation Test, Proceedings of the American Society for Composites 17th Technical Conference, West Lafayette, IN, 2002.

19. D.L. Hunston, W.G. McDonough, G.A. Holmes, R. Parnas, Test Protocol for Single-Fiber Fragmentation Test, http://www.hunstonscientific.com/index_htm_files/InterfaceRR.pdf (Accessed 12 February 2021)

20. A. Awal, G. Cescutti, S.B. Ghosh, J. Müssig, Interfacial studies of natural fibre/polypropylene composites using single fibre fragmentation test (SFFT), Compos. Part A Appl. Sci. Manuf., 42(1): 50–56, 2011.

21. L. Zhou, J.K. Kim, C. Baillie, Y.W. Mai, Fracture Mechanics Analysis of the Fibre Fragmentation Test, J. Compos. Mater., 29(7): 881–902, 1995.

22. S. Deng, L. Ye, Y.W. Mai, H.Y.Liu, Evaluation of fibre tensile strength and fibre/matrix adhesion using single fibre fragmentation tests, Compos. Part A Appl. Sci. Manuf., 29(4): 423–434, 1998.

23 T. Ohsawa, A. Nakayama, M. Miwa, A. Hasegawa, Temperature dependence of critical fiber length for glass fiber-reinforced thermosetting resins. J. Appl. Polym. Sci. 22, 3203–3212. https://doi.org/10.1002/app.1978.070221115, 1978.

24. E. Yongsung, B. Louis, M.Véronique, S. Paul, M. Jan-Anders, Stress-initiated void formation during cure of a three-dimensionally constrained thermoset resin, Polym. Eng. Sci., 41(3): 492–503, 2004.

25. D. Tripathi, A. Kettle, N. Lopattananon, A. Beck, F.R. Jones, Interface molecular engineering of carbon-fiber composites, Compos. Part A Appl. Sci., 30(1):49-57, 1999.

26. R. Gill, “Igneous rocks and processes: A practical guide”, 2nd ed. pp. 20-64, Wiley-Blackwell, Oxford, 2010.

Table 1: Material properties of basalt fibre and epoxy (material data sheets).

Property	13 µm Basalt Fibre	Epoxy Resin
Elastic Modulus (MPa)	90,000	3,400
Tensile Strength (MPa)	3,100	75
Poisson's Ratio	0.26	0.33
Elongation at break (%)	3.5	5 – 6.5

Table 2: Results of fibre diameter measurements using Infinity 2 camera.

Sample No.	Avg. (µm)	Sample No.	Avg. (µm)	Sample No.	Avg. (µm)
1	13.20	**4**	n/a	**7**	12.31
2	13.09	**5**	n/a	**8**	15.27
3	damaged	**6**	13.40	**9**	15.07

Table 3: Fibre breaks vs load increment (F= failure occurred).

Load Increment	21	22	23	24	25	26	27	28	29	30	31	32
Fibre Breaks for sample 2	1	2	2	F								
Fibre Breaks for sample 6	0	F										
Fibre Breaks for sample 7	0	1	1	1	1	1	1	2	2	2	2	F

Table 4: Number of breaks and fibre fragment lengths in each sample.

Sample No.	No. of Breaks	Fragment Length (mm)			
		Break 1-2	Break 2-3	Break 3-4	Break 4-5
1	3	1.695	5.384	n/a	n/a
2	3	1.190	0.752	n/a	n/a
7	4	1.305	2.015	1.650	n/a
8	6	1.110	1.420	1.531	3.325
9	4	0.752	1.882	1.101	n/a

Table 5: Different failure modes of each break observed.

Sample No.	**Fibre Break Failure Mode Type**				
	Break 1	**Break 2**	**Break 3**	**Break 4**	**Break 5**
1	(b)	(b)	(a)	n/a	n/a
2	(a)	(b)	(b)	n/a	n/a
7	(b)	(a)	(b)	(a)	n/a
8	(b)	(a)	(a)	(a)	(a)
9	(c)	(a)	(b)	(b)	n/a

Table 6: Test temperatures and other testing values determined from data files.

Sample No.	**Test Temp. (°C)**	**Max Load (N)**	**Max Disp. (mm)**	**U.T.S. (MPa)**	**Failure Strain (%)**	**Elastic Modulus (MPa)**
1	20	402.67	1.31	72.93	6.56	1510.3
2	20	444.55	1.04	61.80	5.18	1455.4
4	19	419.58	1.06	68.39	5.32	1638.5
7	19	474.35	1.27	74.80	6.37	1670.0
8	20	484.82	1.28	82.45	6.39	1720.3
9	20	469.52	1.29	81.57	6.43	1740.6

Table 7: Theoretical interfacial shear strength values.

Sample No.	2	7	FE model
τ_i (MPa)	9.0451	9.7708	19.0407

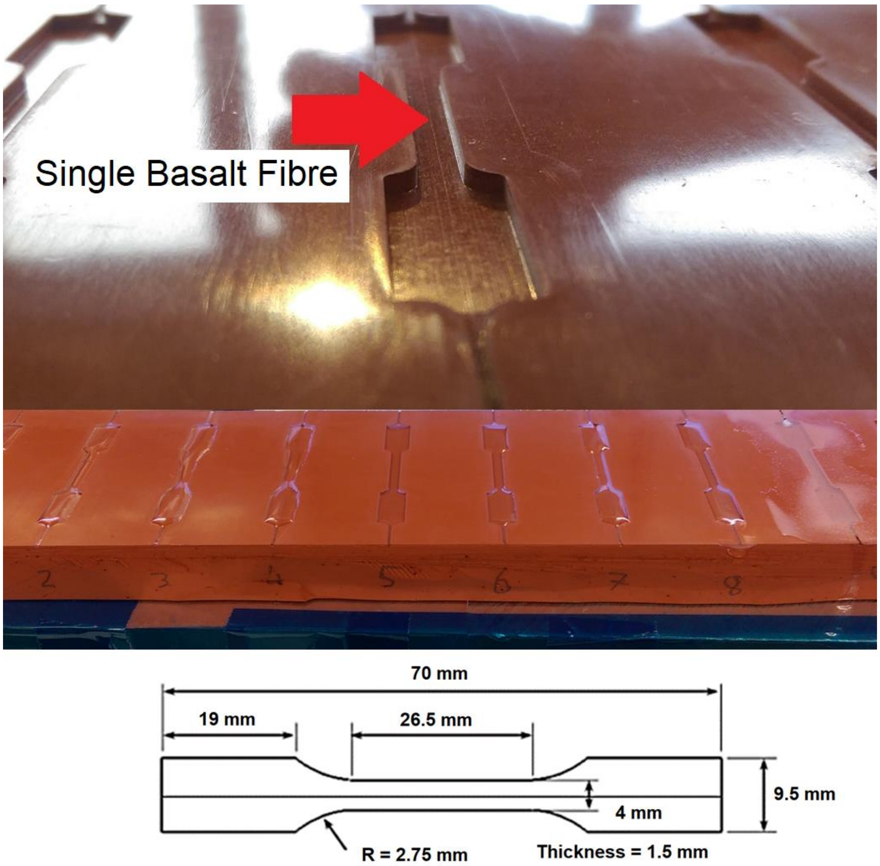

Figure 1: Sample manufacturing and approximate dimensions of samples.

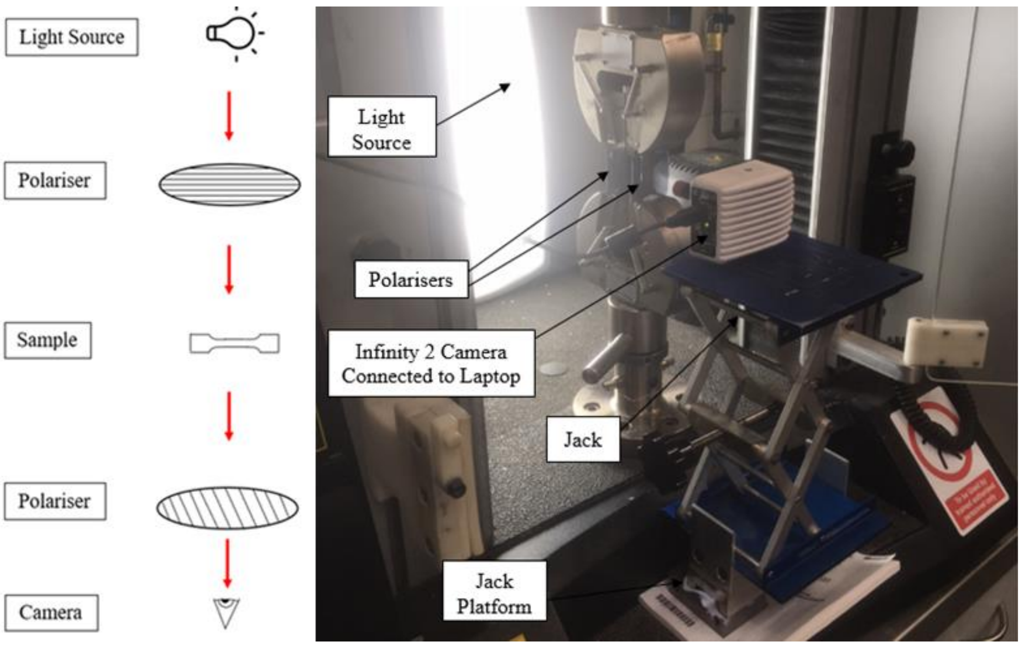

Figure 2: Experimental testing diagram and setup.

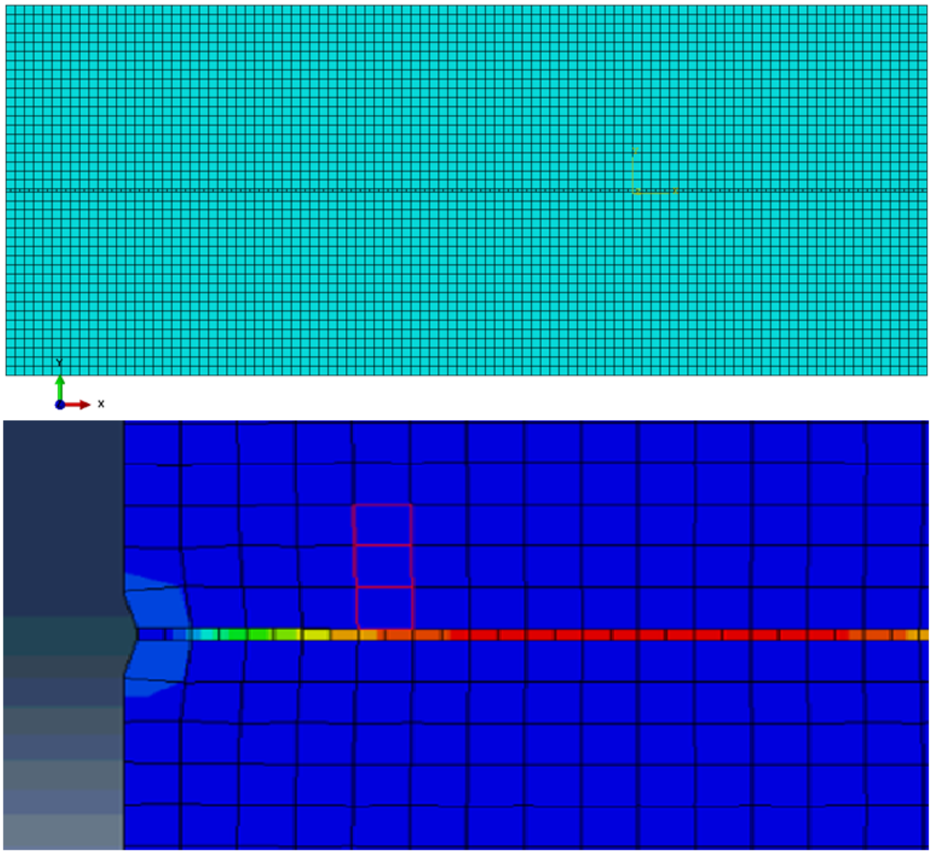

Figure 3: The increment convergence study.

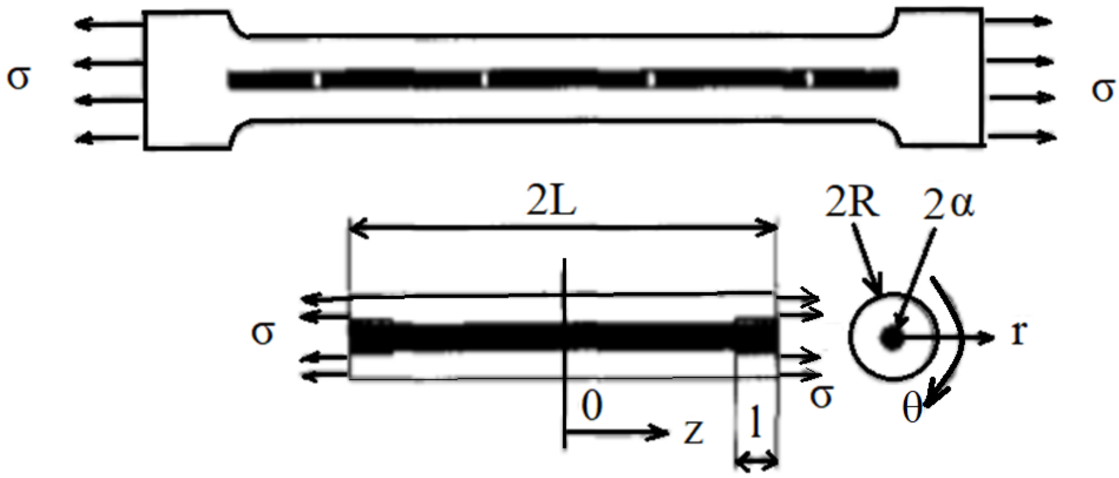

Figure 4: Schematic diagram of parameters required for theoretical model.

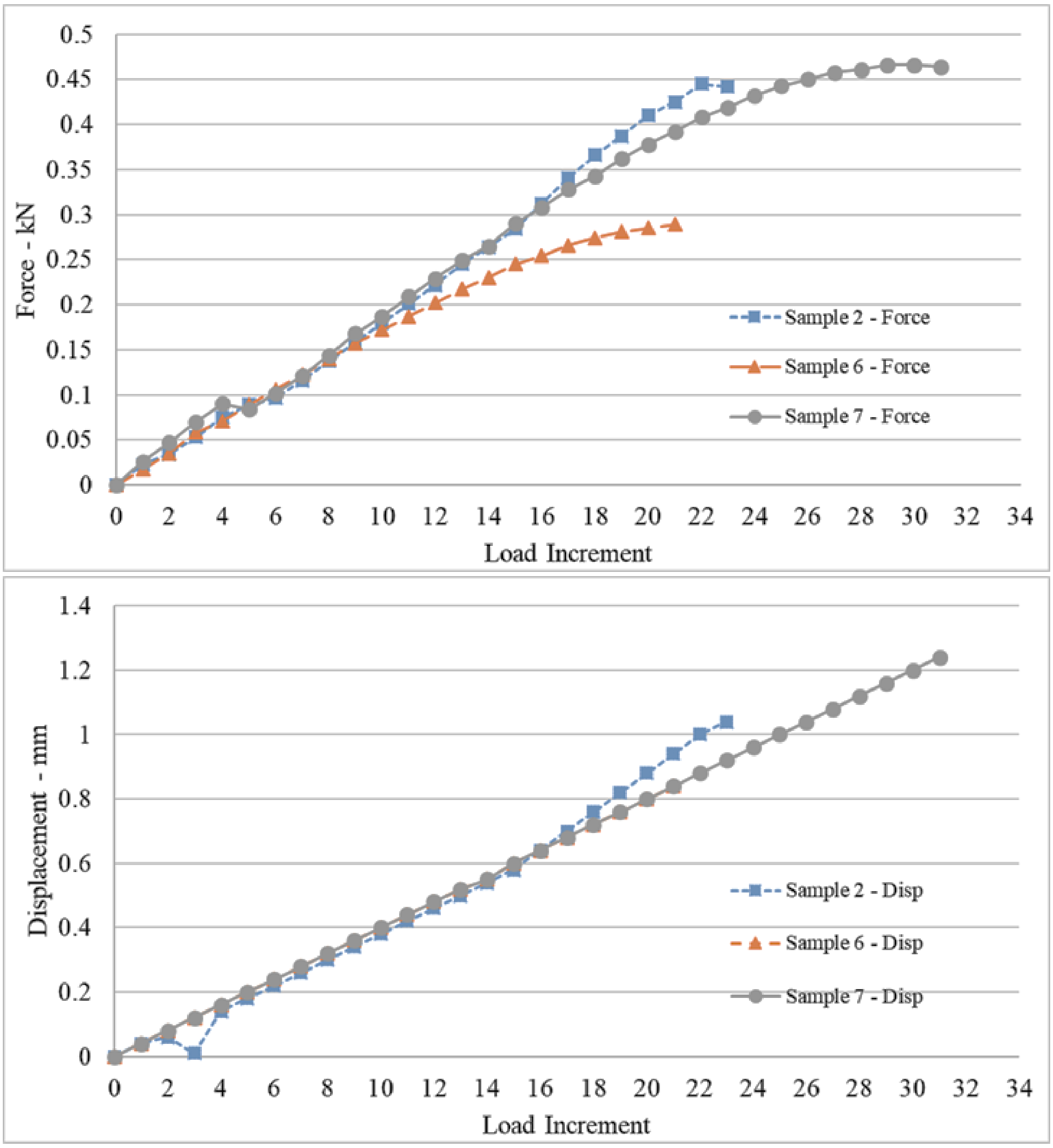

Figure 5: Recorded force and displacement values after each incremental loading step

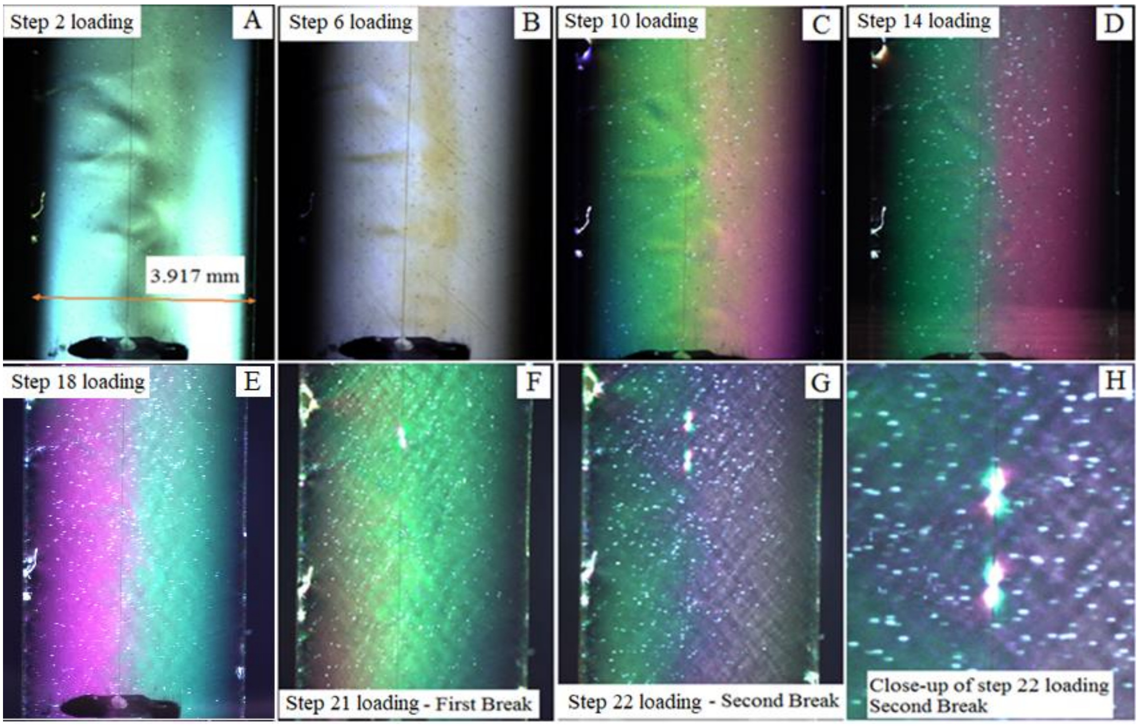

Figure 6: Sample 2 images in different loading steps.

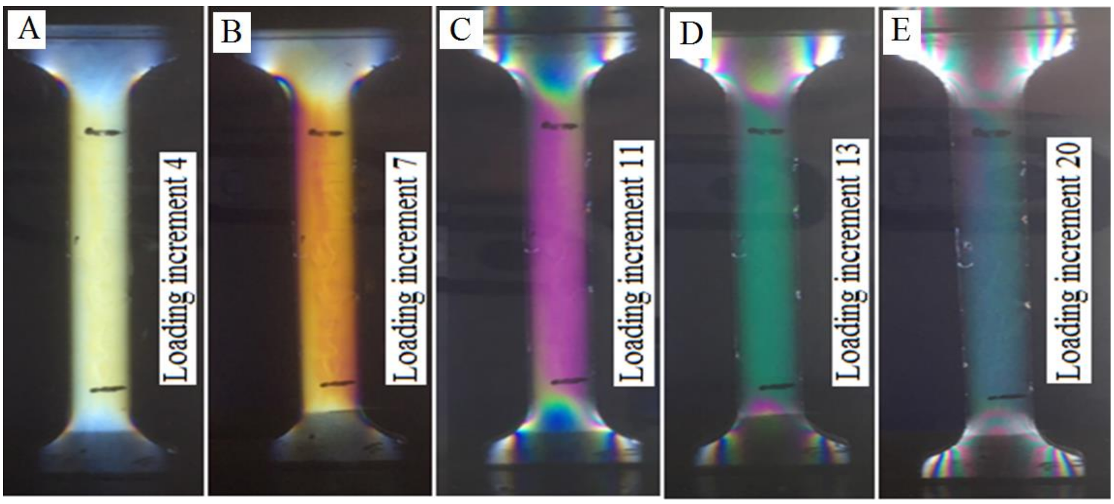

Figure 7: Stress-induced birefringence of sample 2 after different loading increments.

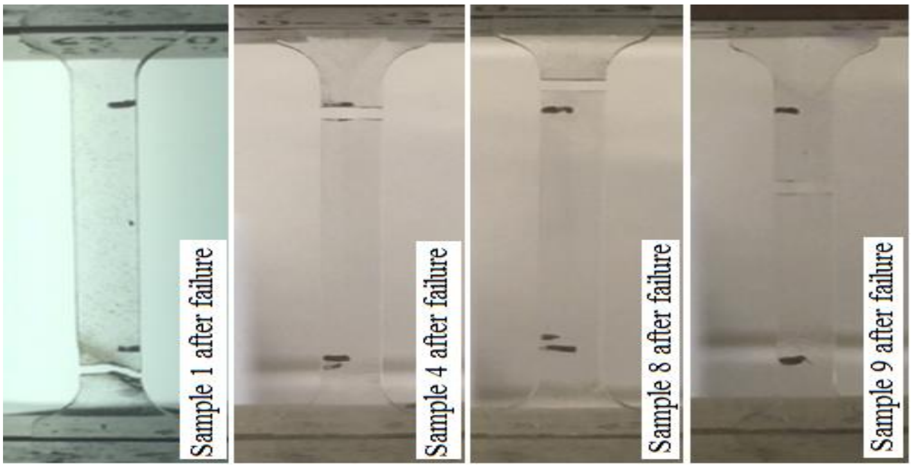

Figure 8: samples 1, 4, 8, and 9 (continuous loading) after failure

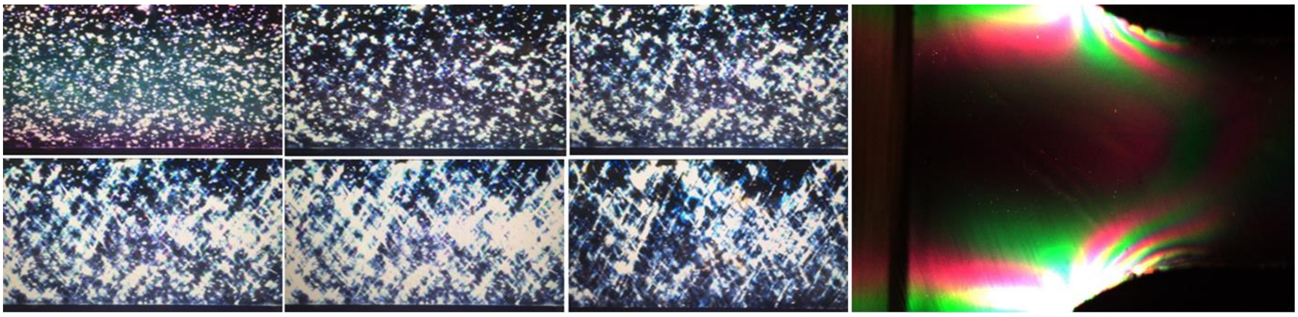

Figure 9: Sample 1 imperfections under different loads (Left), Stress-induced birefringent patterns in grip region of sample 2 (Right).

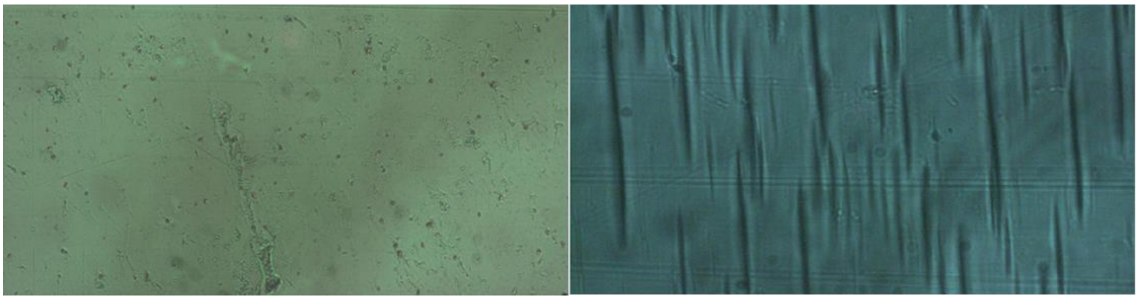

Figure 10: Sample surface before (left) and after (right) testing.

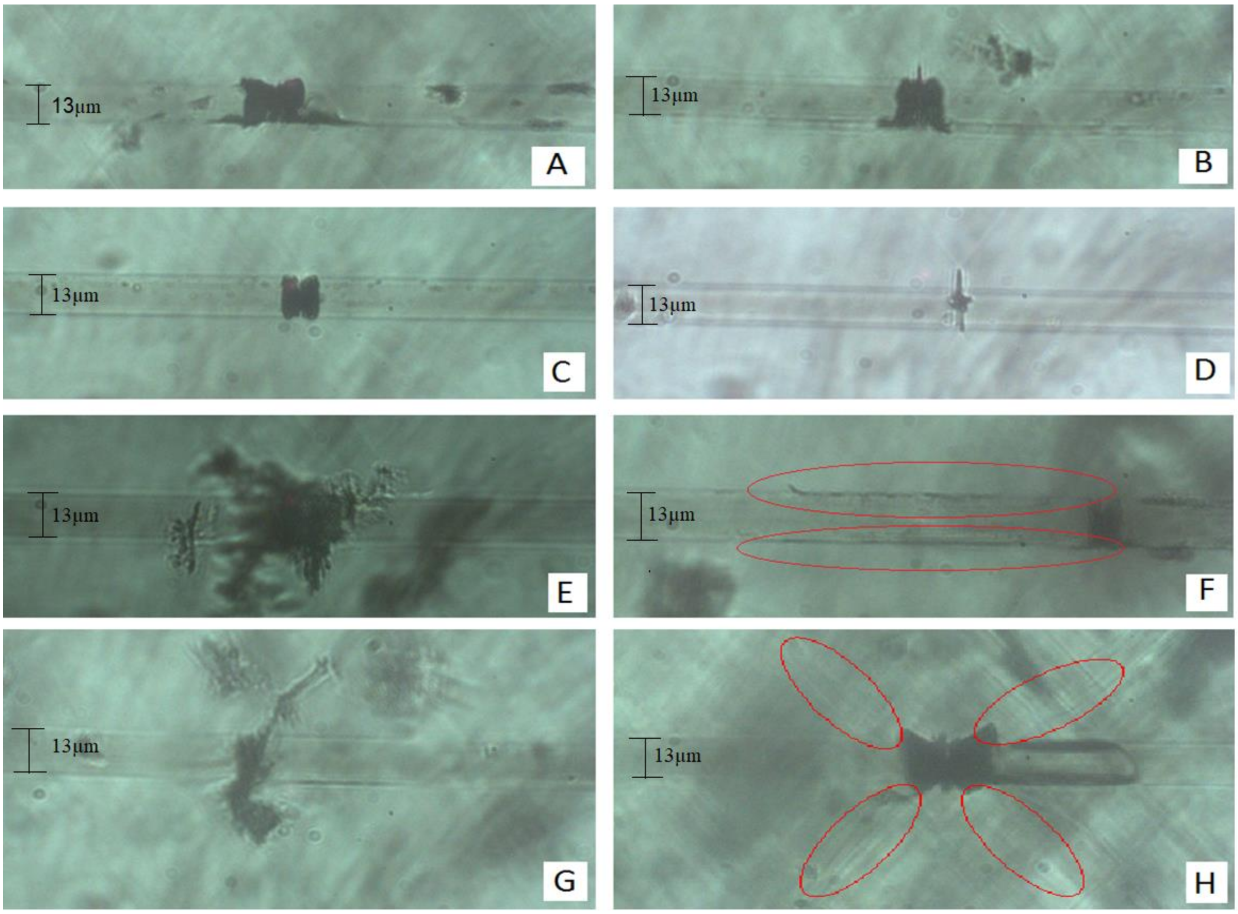

Figure 11: A) Failure mode (b) in sample 1 with some interfacial debonding, B) Failure mode (b) in sample 1 with small amount of interfacial debonding and slight transverse matrix crack, C) Failure mode (b) in sample 2, D) Failure mode (a) in sample 7, E) Failure mode (a) in sample 8 with crack propagation towards microscope lens, F) Failure mode (c) in sample 9, G) Failure mode (a) in sample 9, H) Failure mode (b) in sample 9 with moderate interfacial debonding.

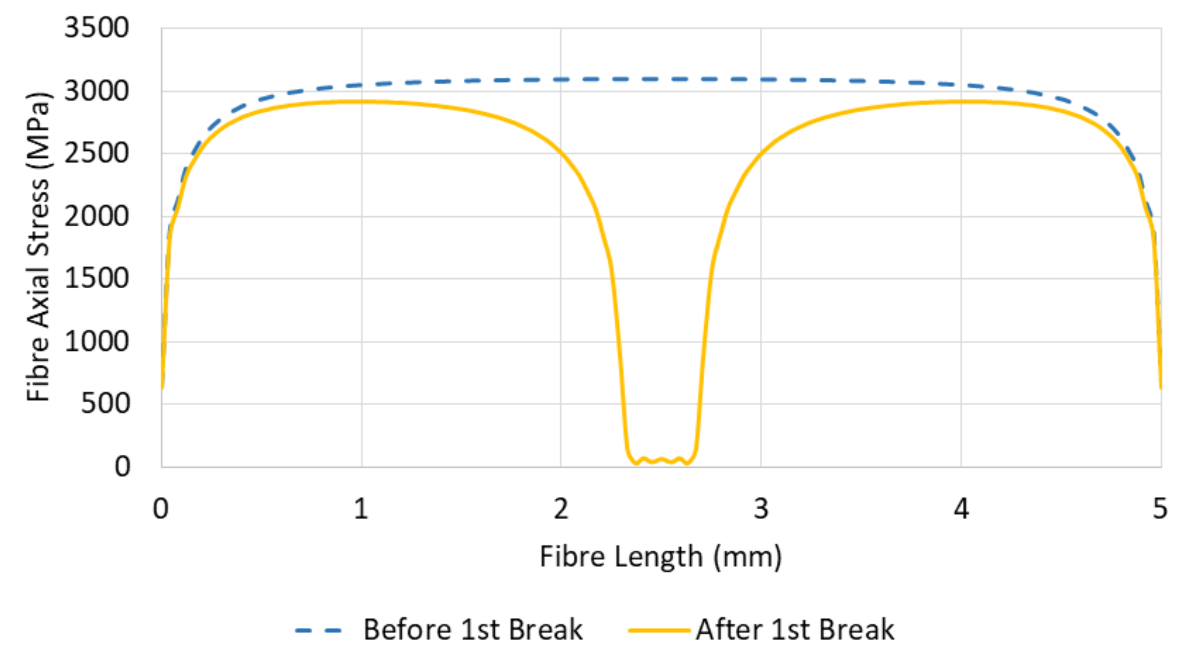

Figure 12: S11 stress in FE model (Left), FE predicted fibre axial stress (Right) before and after the first fibre break.

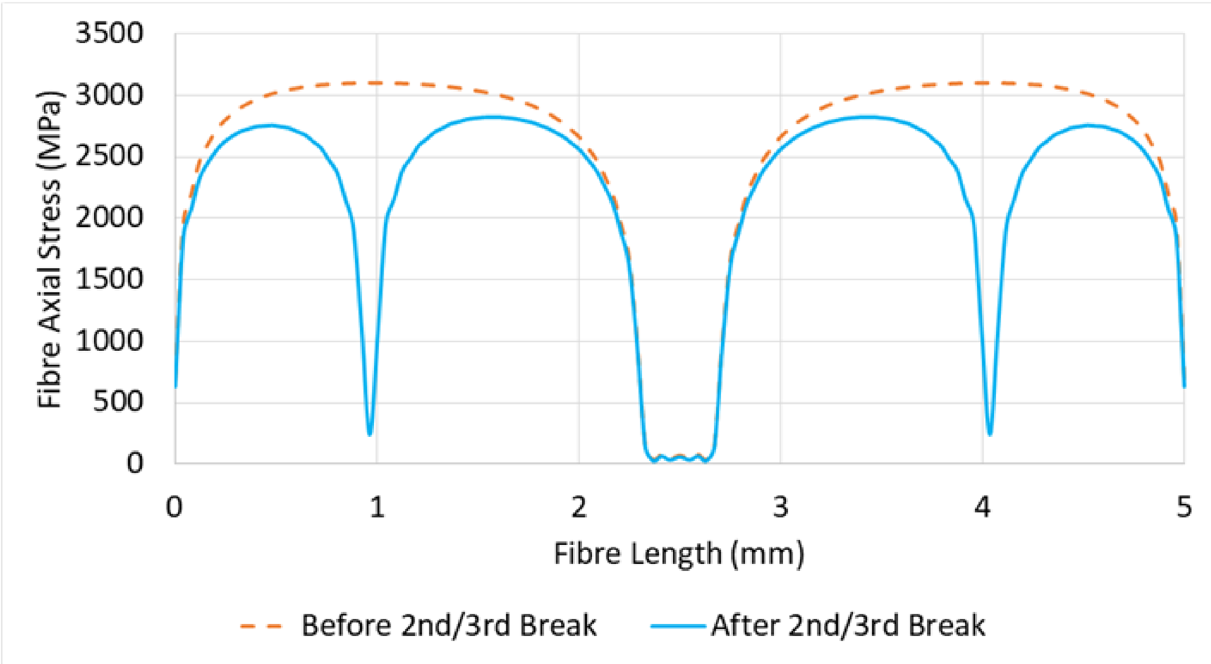

Figure 13: S11 stress in FE model (Left), FE predicted fibre axial stress (Right) before and after the second and third fibre breaks.

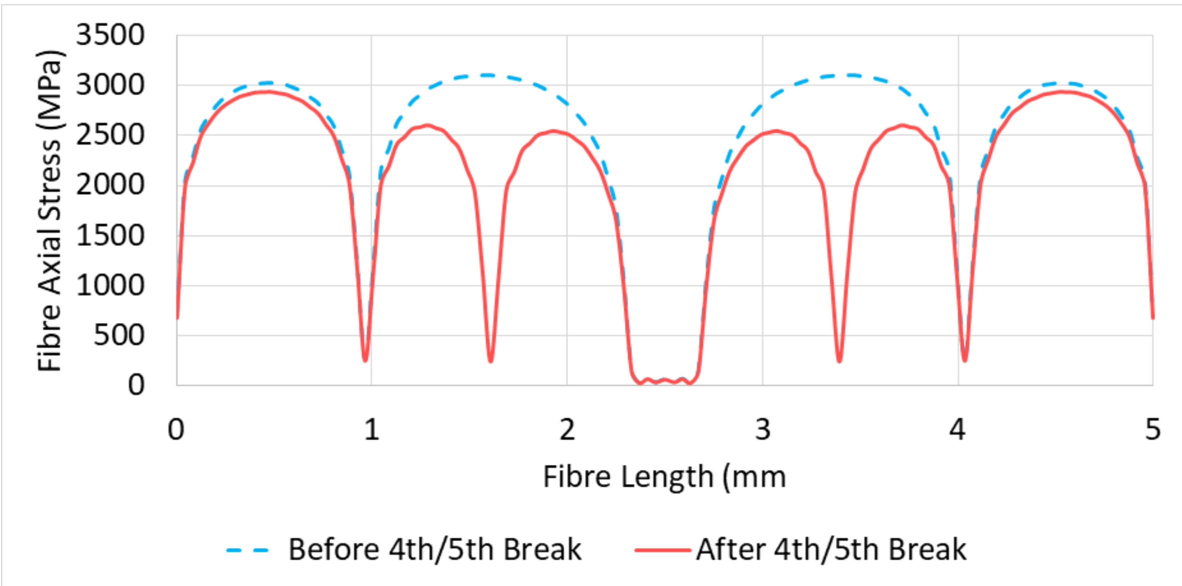

Figure 14: S11 stress in FE model (Left), FE predicted fibre axial stress (Right) before and after the fourth and fifth fibre breaks.

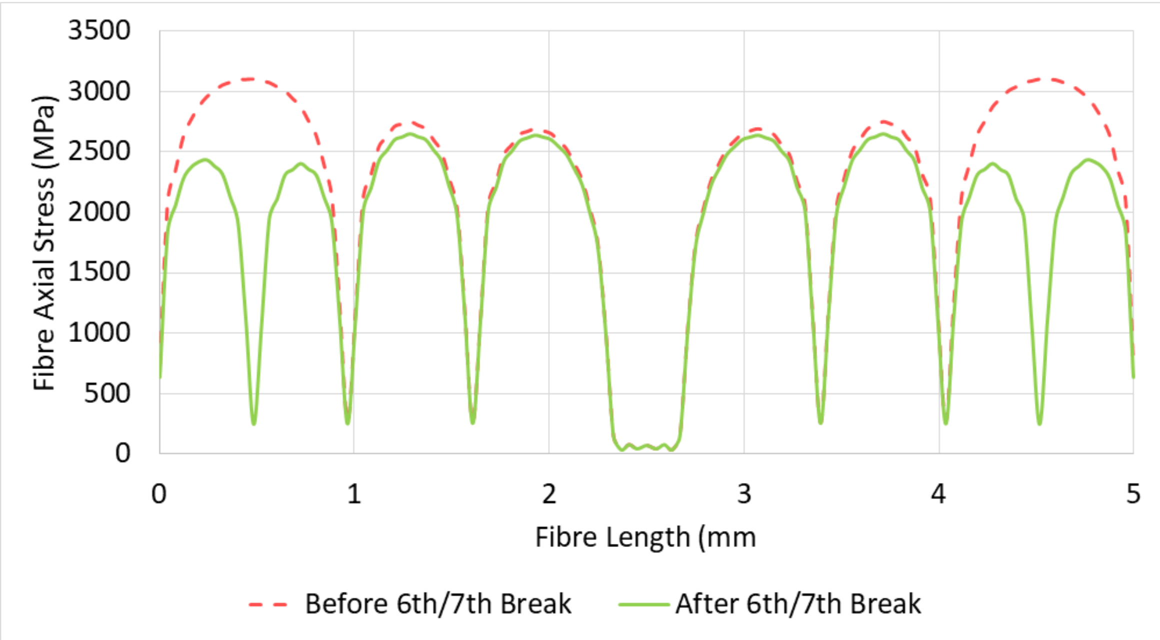

Figure 15: S11 stress in FE model (Left), FE predicted fibre axial stress (Right) before and after the sixth and seventh fibre breaks.

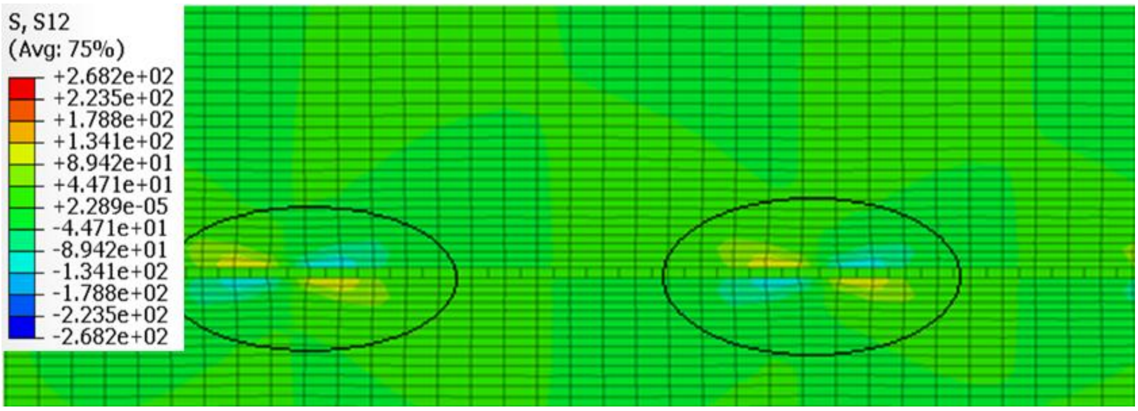

Figure 16: Close-up image of shear stresses about fibre fractures in FE model.

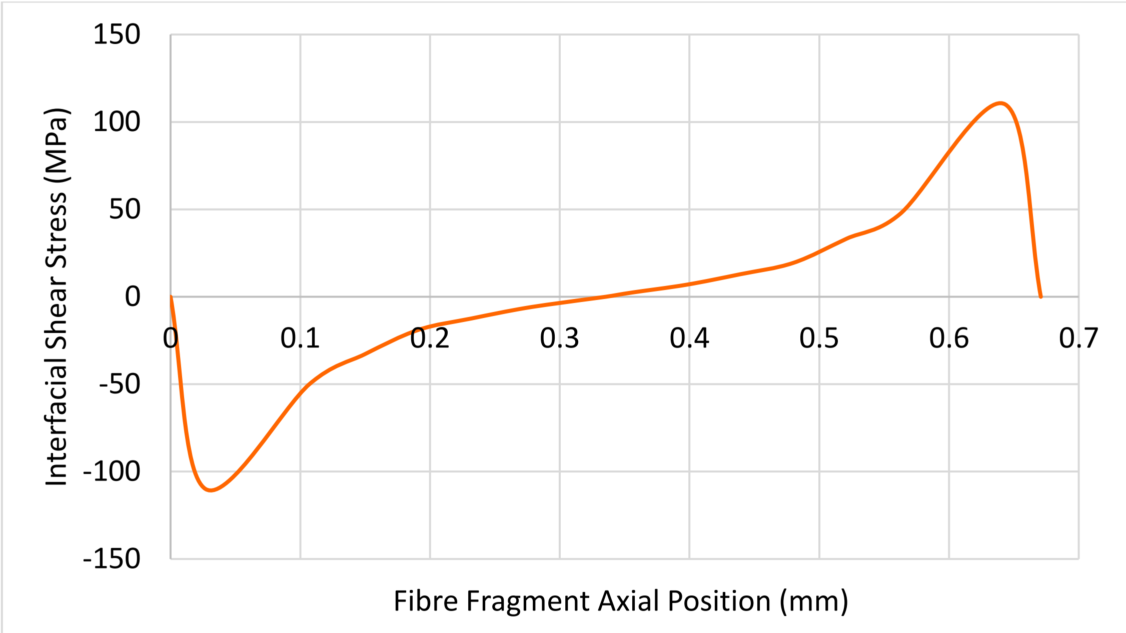

Figure 17: FE predicted interfacial shear stress distribution for fibre fragment.

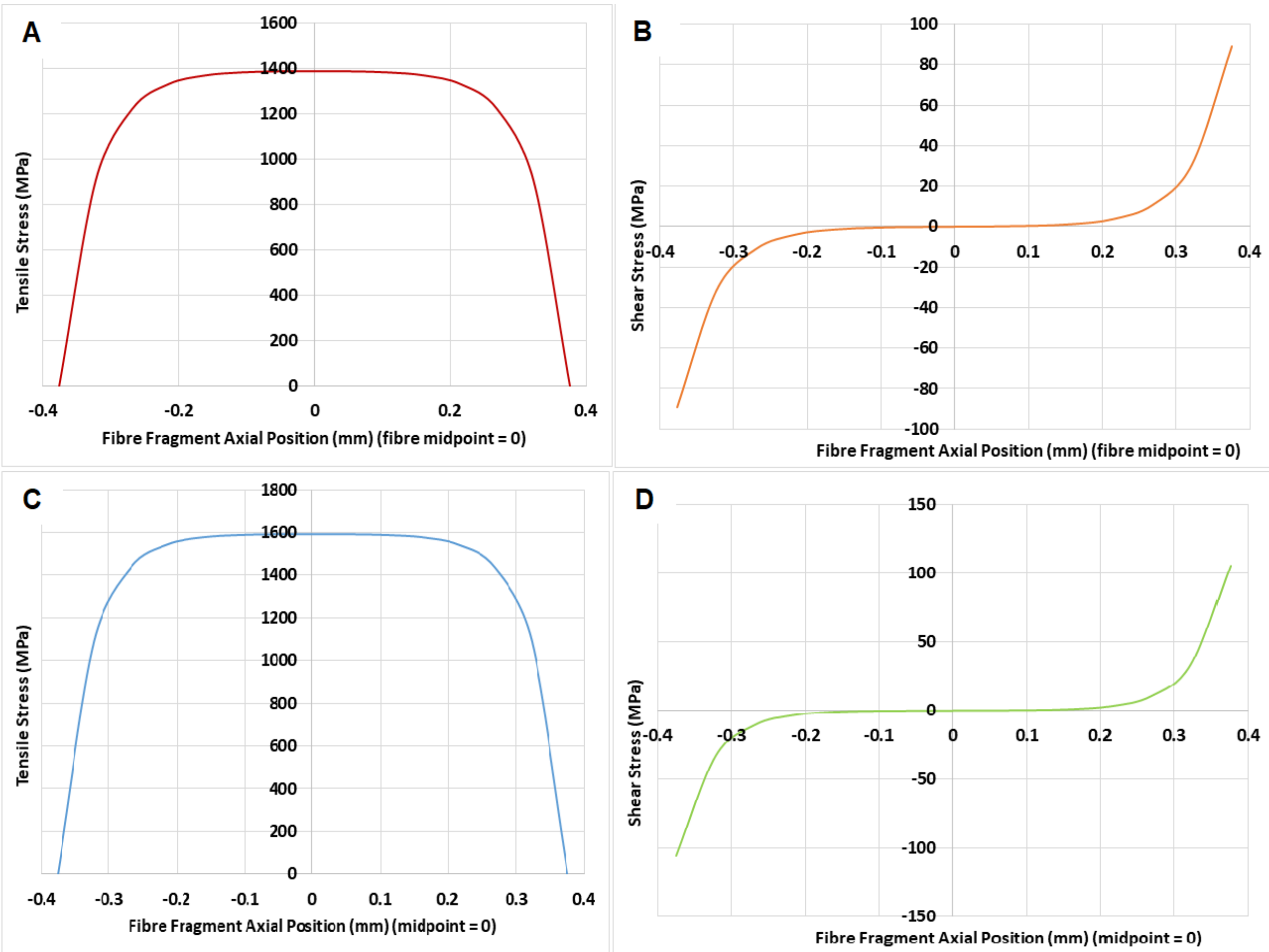

Figure 18: Theoretical prediction of fibre fragment tensile stress as a function of fibre axial position for sample 2 (A), sample 2 (B), sample 7 (C) and sample 7 (D).

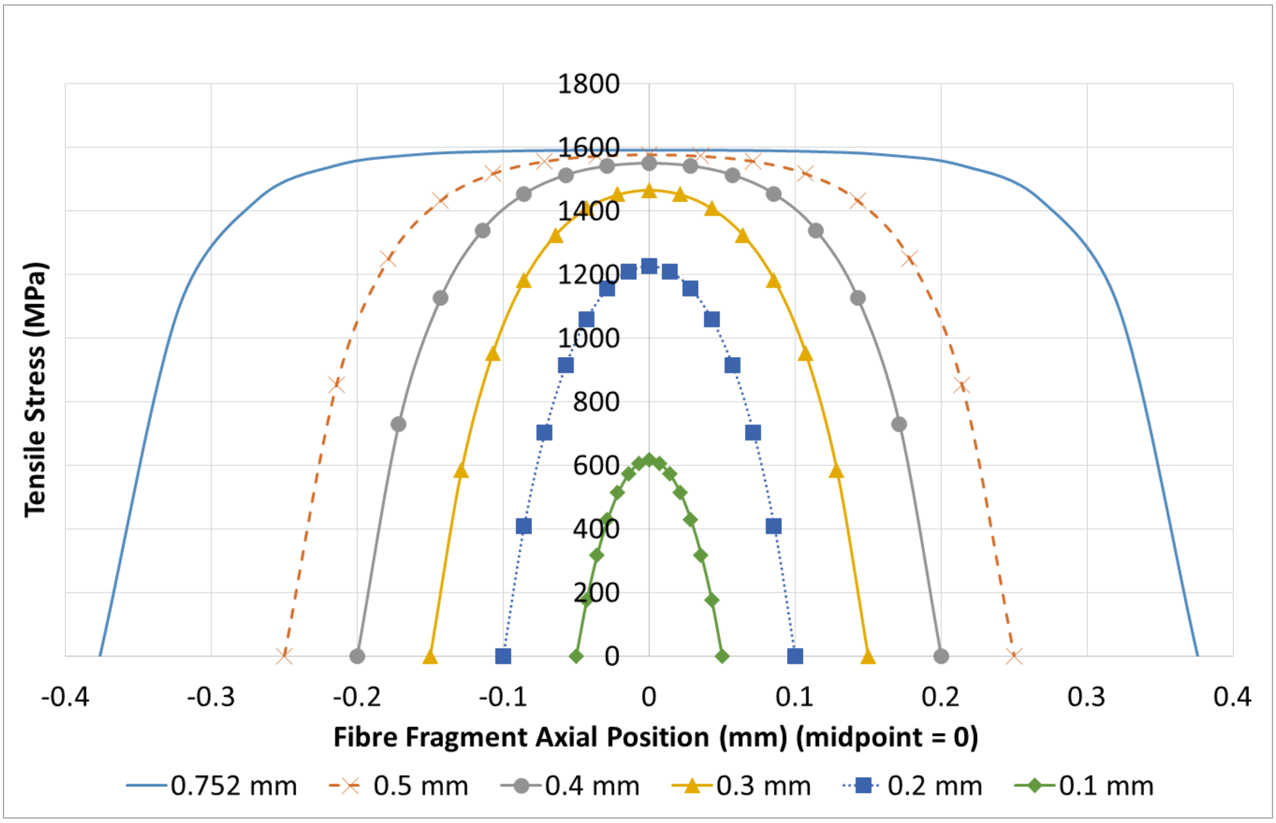

Figure 19: Axial stress distribution for fibres of various lengths.